Breast Cancer: Targets and Therapy

Dovepress
Taylor & Francis Group

Open Access Full Text Article

ORIGINAL RESEARCH

Discrimination of Triple-Negative Breast Cancer: A Robust Clinical Baseline versus Multimodal Magnetic Resonance Imaging Integrated Models with Assessment of Generalizability

Xueyan Liao[1], Xiaomin Wu[1], Junqiong Zheng[2], Guoliang Lin[3], Dandan Lin[1]

[1]Department of Radiology, Longyan First Affiliated Hospital of Fujian Medical University, Longyan, Fujian, 364000, People's Republic of China; [2]Department of Medical Oncology, Longyan First Affiliated Hospital of Fujian Medical University, Longyan, Fujian, 364000, People's Republic of China; [3]Department of Surgical Oncology, Longyan First Affiliated Hospital of Fujian Medical University, Longyan, Fujian, 364000, People's Republic of China

Correspondence: Dandan Lin; Xiaomin Wu, Department of Radiology, Longyan First Affiliated Hospital of Fujian Medical University, No. 105, Jiuyi North Road, Xinluo District, Longyan, Fujian, 364000, People's Republic of China, Email ldd1232025@126.com; m19942754796@163.com

Objective: This study aims to compare the potential performance of multimodal MRI-based models in discriminating TNBC.

Methods: Clinical and MRI data from 162 female breast cancer patients diagnosed at our hospital between March 2022 and June 2024 were retrospectively collected. Clinical-conventional MRI model, qMRI model, radiomics model, and three integrated models were constructed on the borderline SMOTE-processed training set. ROC and DCA analyses were used to evaluate the discrimination performance and clinical net benefit. The optimal model was selected by validating the stability of the integrated models on the test set.

Results: The mean age of 162 patients was 50.549 ± 9.563 years. No significant differences were found between the training set (n = 113) and the test set (n = 49) (all $P > 0.05$). The performance of models on the borderline SMOTE-processed training set was as follows: the clinical-conventional MRI model (including Ki-67 and BPE) achieved an AUC of 0.896; the qMRI model (including ADC_{tunor} and T2-mapping $_{tumor)}$ achieved an AUC of 0.781; the radiomics model (including 9 key features) achieved an AUC of 0.905. The fully integrated model (clinical-conventional MRI model integrating all multimodal features) demonstrated optimal performance (AUC: 0.986). However, during independent validation in the test set, the fully integrated model's AUC decreased to 0.718, while the clinical-conventional MRI model maintained relatively stable discriminatory performance (AUC: 0.862).

Conclusion: The clinical-conventional MRI model demonstrated stable discriminatory performance. While complex models show potential, their ability to generalize was limited by sample size, highlighting the need for validation with larger datasets.

Keywords: triple-negative breast cancer, magnetic resonance imaging, radiology, model

Introduction

Breast cancer is the most common malignant tumour among women globally, posing a serious threat to female health.[1] Among these, triple-negative breast cancer (TNBC) is a unique subtype defined by the lack of expression of the estrogen receptor (ER), progesterone receptor (PR), and human epidermal growth factor receptor 2 (HER2).[2] TNBC accounts for approximately 15–20% of all breast cancer cases, yet contributes to 30–40% of breast cancer-related deaths.[3] This subtype typically exhibits adverse clinical characteristics, including high aggressiveness, elevated early recurrence rates, metastatic propensity, and poor overall survival.[4] Its considerable heterogeneity is a key factor underpinning substantial variations in treatment response and prognosis.[5] Currently, TNBC treatment remains primarily reliant on chemotherapy. However, the lack of specific molecular targets often results in limited treatment options and a higher risk of drug resistance, posing significant challenges in clinical management.[6] Therefore, accurately identifying and stratifying the risk of TNBC are crucial steps in advancing personalized treatment and enhancing patient outcomes.

https://doi.org/10.2147/BCTT.S594356
Received: 29 January 2026
Accepted: 21 March 2026
Published: 2 April 2026

In recent years, artificial intelligence (AI) has achieved remarkable progress in the field of TNBC imaging diagnosis. Models based on deep learning and radiomics have demonstrated outstanding performance in TNBC detection, molecular subtyping, and prognostic assessment.[7] For instance, Huang et al utilised multiparametric magnetic resonance imaging (MRI) techniques and samples from 188 breast cancer patients, demonstrating that integrating radiological features into machine learning classifiers could characterise TNBC with a natural diagnosis of 0.86.[8] A hybrid deep learning model based on mammography achieved 74.8% accuracy in classifying TNBC as HER2-enriched.[9] These findings fully demonstrate the immense potential of artificial intelligence technologies in enhancing the precision of TNBC diagnosis and treatment.

In breast cancer imaging, MRI is currently recognised as the most sensitive modality. Recent advancements in radiomics models based on breast MRI have significantly improved the ability to differentiate between benign and malignant breast tumors[10,11] and identify distinct molecular subtypes.[12,13] Medical imaging plays an irreplaceable role throughout the TNBC diagnosis and treatment pathway. Dynamic contrast-enhanced MRI (DCE-MRI) can reveal TNBC-related imaging features, such as tumour size, margin morphology, and enhancement patterns, providing crucial evidence for precise diagnosis and treatment planning.[14] However, overlapping DCE time-signal curves across different breast lesions may elevate false-positive rates and complicate diagnosis.[15] To address this limitation, quantitative MRI (qMRI) techniques have gained importance, including relaxation-based mapping (eg., T1, T2 mapping),[16] magnetic resonance spectroscopy (MRS),[17] and diffusion MRI [including diffusion-weighted imaging (DWI) and derived parameters]. These methods have been shown to effectively discriminate between benign and malignant breast lesions.[18] Synthetic MRI (SyMRI), a new qMRI technique, offers significant advantages: it quickly generates quantitative T1 and T2 maps in a single scan, taking only minutes-much shorter than traditional qMRI scan times.[19] At the same time, as a non-invasive, cost-effective, and multi-parametric predictive tool, radiological features extracted from MRI show great potential in distinguishing between benign and malignant breast lesions.[20] As an important branch of quantitative medical imaging analysis, radiomics uses computational algorithms to extract quantitative features from images that are difficult for the human eye to detect. These features are then correlated with clinical parameters to aid in clinical decision-making.[21] However, due to the relatively low prevalence of TNBC within the overall breast cancer population, dedicated radiomics scoring studies specifically targeting TNBC are currently limited.[22]

Although the aforementioned multimodal MRI techniques each demonstrate considerable potential, current research remains largely confined to single-modality investigations. How to effectively integrate the macroscopic information from clinical MRI, the functional information from quantitative mapping, and the microscopic heterogeneity information from radiomics to construct a robust and efficient model for accurately distinguishing TNBC and predicting its key clinical outcomes remains a significant gap and challenge in the current research field. Based on this, this study aims to develop a comprehensive analysis strategy based on multimodal MRI. We propose integrating routine clinical MRI sequences, qMRI mapping parameters, and radiomics features to establish a robust discrimination model. This aims to provide a novel, non-invasive imaging solution for the precise identification, risk stratification, and treatment decision-making of TNBC, ultimately advancing the progress of personalised precision medicine for this disease.

Methods

Study Population

This retrospective study analyzed the clinical and imaging data of 162 female breast cancer patients diagnosed at Longyan First Hospital, Fujian Province, between March 2022 and June 2024. Inclusion criteria were: (1) Breast cancer confirmed by surgical pathology with a single mass lesion larger than 1 centimeter (cm) in maximum diameter; (2) Patients underwent breast MRI and obtained apparent diffusion coefficient (ADC) maps, native T1 relaxation time maps (T1 mapping), T2 relaxation time quantitative maps (T2 mapping), and post-contrast T1 relaxation time quantitative maps (ΔT1 mapping); (3) No prior needle biopsy, surgical resection, radiotherapy, chemotherapy, hormonal therapy, or targeted therapy before MRI examination; (4) Complete pathological data allowing for breast cancer molecular subtyping. Exclusion criteria: (1) Poor image quality failing to meet analysis requirements; (2) Pregnancy or lactation.

Histopathological Analysis

Postoperative histopathological specimens were analyzed by experienced breast pathologists. All immunohistochemical and molecular assessments strictly adhered to the Chinese Anti-Cancer Association Breast Cancer Diagnosis and Treatment Guidelines and Standards (2024 Edition),[23] with specific positivity criteria as follows: ER and PR require nuclear staining >1%; HER2 requires 3+ membrane staining or FISH positivity; the Ki-67 proliferation index uses 30% as the cutoff value.[24–26] Based on these criteria, breast cancer is classified as Luminal A type (ER/PR+, HER2-, and Ki-67 < 30%), Luminal B type ([ER/PR+, HER2-, and Ki-67 ≥30%] or [ER/PR+, HER2+, and Ki-67 at any level]), HER2-overexpressing type (ER-, PR-, and HER2+), and TNBC (ER-, PR-, HER2-). Among the 162 patients, there were 134 cases of non-TNBC and 28 cases of TNBC.

MRI Examination methods and Parameters

MRI data were acquired using a Philips 3.0T scanner equipped with a 16-channel breast coil. Participants were positioned prone with their heads first, allowing both breasts to naturally hang in the center of the coil. The scanning protocol included conventional static sequences [T1-weighted imaging (T1WI), T2-weighted imaging (T2WI), and DWI], DCE sequences (using gadopentetate dimeglumine), and quantitative imaging sequences (T1 mapping and T2 mapping). All sequence parameters are detailed in Table S1.

Image Postprocessing

Region-of-Interest (ROI) Annotation

All data were evaluated by two radiologists. ① By combining T1WI, T2WI, and DWI images, the lesion boundaries and extent were determined, and an ROI labeled "tumor" was outlined along the margin on the plane with the largest lesion size (ROI range: 1.0–6.5 cm^2); ② A second ROI labeled "local" was delineated within the region showing the most pronounced tumor enhancement, avoiding areas of hemorrhage, necrosis, or cystic changes (ROI size ranged from 0.5 to 2.5 cm^2 depending on tumor size). The consistency of quantitative parameter measurements between the two radiologists was relatively high (Intraclass correlation coefficient (ICC) > 0.8).

Data Acquisition for Mapping

The following parameters were measured for both tumor and local ROIs in each patient: T1 mapping (pre-contrast), T2 mapping, ADC value, ΔT1 mapping (post-contrast), and ΔT% (= (T1 mapping - ΔT1 mapping) / T1 mapping, representing the relative change rate of T1 mapping relaxation time between pre- and post-contrast scans. Figure 1A–H illustrates the data extraction process.

Radiomics Feature Extraction

All images were manually segmented and annotated using the free open-source software package (3D Slicer, version 3.4.0) to delineate ROIs encompassing the entire tumour volume, including necrotic areas. Radiomics feature extraction was performed using the built-in radiomics module within 3D Slicer, developed based on the PyRadiomics platform.[27] To ensure stability and reproducibility in feature computation, this study strictly adhered to standardised operating procedures: images were not resampled before feature extraction to preserve native resolution information; grey-level binning employed a fixed bin width of 25. All parameters were configured according to the official PyRadiomics default settings (https://pyradiomics.readthedocs.io/en/latest/index.html). The ICC value exceeds 0.8. Each segmented lesion yielded 837 features, categorized into the following six groups: (1) 162 first-order (FO) features; (2) 216 gray level co-occurrence matrix (GLCM) features; (3) 126 gray level dependence matrix (GLDM) features; (4) 144 gray level run length matrix (GLRLM) features; (5) 144 gray level size zone matrix (GLSZM) features; and (6) 45 neighboring gray tone difference matrix (NGTDM) features. To eliminate feature scale differences and improve model convergence, all extracted radiometric features were normalized using z-score normalization before further analysis.

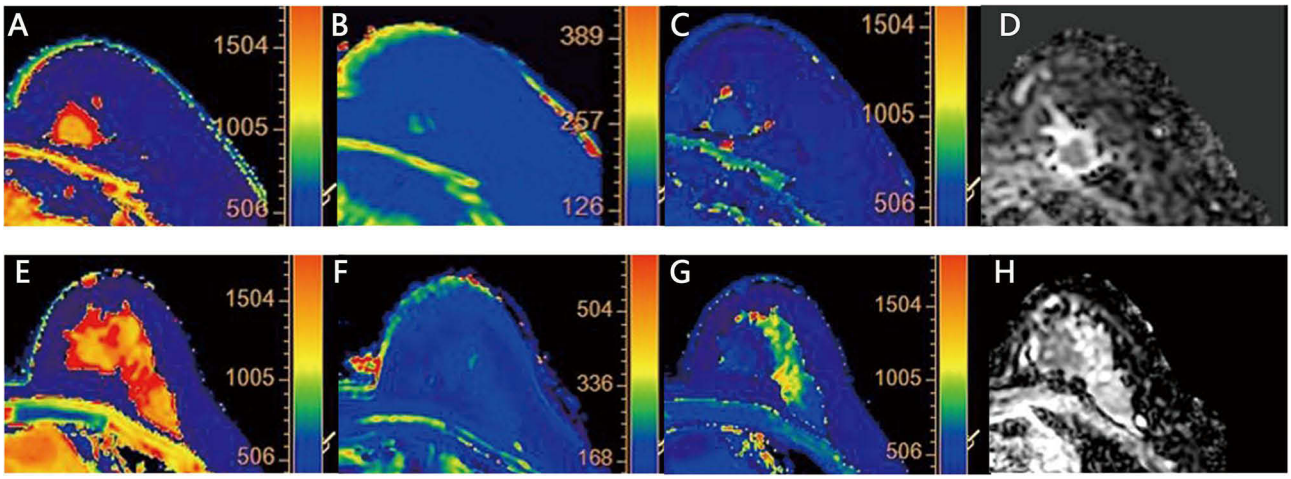

Figure 1 T1 mapping (**A**), T2 mapping (**B**), ΔT1 mapping (**C**), and ADC map (**D**) of a TNBC patient; T1 mapping (**E**), T2 mapping (**F**), ΔT1 mapping (**G**), and ADC map (**H**) of a non-TNBC patient.
Abbreviations: ADC, Apparent diffusion coefficient; TNBC, Triple-negative breast cancer.

Clinical Data Collection

The following data were collected from electronic medical records: (1) clinical characteristics: age (years), Ki-67 index (%), and histological grade; (2) conventional MRI imaging features: shape, fibroglandular type, background parenchymal enhancement (BPE), signal time-intensity curve (TIC), and maximum diameter (mm); and (3) qMRI imaging data: T1 $mapping_{tumor}$, T2 $mapping_{tumor}$, ΔT1 $mapping_{tumor}$, ADC $_{tumor}$ (10^{-6}), ΔT $_{tumor}$(%), T1 $mapping_{local}$, T2 $mapping_{local}$, ΔT1 $mapping_{local}$, ADC $_{local}$ (10^{-6}), and ΔT $_{local}$ (%).

Data Split

To mitigate overfitting, the dataset was divided into a training set and a test set in a 7:3 ratio. The division was based on the stratified classification of TNBC and non-TNBC states, with other clinical data being randomly assigned. The training set was utilized for feature selection and model development, while the test set was employed to assess model performance. Due to the limited number of positive samples, data imbalance could affect the discriminative model's performance. We used the borderline synthetic minority over-sampling technique (SMOTE) on the training set to balance the dataset and improve discrimination accuracy.[28] This method builds upon the traditional SMOTE algorithm by specifically targeting minority class samples situated in boundary regions between majority and minority classes-areas prone to misclassification. By generating new samples around these critical instances, borderline SMOTE enhances the classifier's discriminative power, particularly in scenarios where category overlap occurs. To reflect real clinical data distribution, the test set was not treated with borderline SMOTE.

Model Construction and Validation

Initially, three single models were constructed to discriminate TNBC: a clinical-conventional MRI model, a qMRI model, and a radiomics model. Subsequently, based on the clinical-conventional MRI model, we constructed integrated model 1 (clinical-conventional MRI model with qMRI parameters), integrated model 2 (clinical-conventional MRI model with radiomics features), and full integrated model 3 (clinical-conventional MRI model integrating all multimodal features). The discriminatory performance and clinical net benefit of these models were evaluated using receiver operating characteristic curve (ROC) analysis and decision curve analysis (DCA). To further validate model robustness and quantify inter-observer bias, an additional experienced radiologist (independent of the original two) was invited to perform independent, single-slice ROI delineation on all TNBC cases and 28 randomly selected non-TNBC patients, unaware of the original results. Model performance was re-validated based on this new radiologist's delineations.

Additionally, internal validation was performed using 10-fold nested cross-validation on the original training set, whilst model performance stability was also assessed on the original test set.

Statistical Analysis

For the borderline SMOTE-processed training set, Shapiro–Wilk tests were used to check the normality of continuous variables. Normally distributed continuous variables were described by mean ± standard deviation (SD) and compared using *t*-tests. Non-normally distributed continuous variables were described by median [P_{25}, P_{75}] and compared using Mann–Whitney *U*-tests. Categorical variables were described by counts (%) and analyzed using χ^2-tests or Fisher's exact tests. Multicollinearity analysis was performed to exclude variables with a variance inflation factor (VIF) > 10, indicating collinearity. Multivariable logistic regression was employed to identify clinical characteristics, conventional MRI variables, and qMRI variables influencing TNBC.

Least absolute shrinkage and selection operator (LASSO) regression was used to filter radiomics features associated with TNBC. The selected radiomics features were further ranked by importance using XG Boost and Random Forest machine learning algorithms. The top ten overlapping features from both algorithms were chosen as key radiomics features. The Radscore was calculated based on their LASSO regression coefficients. All statistical analyses were conducted using R software, with $P < 0.05$ indicating statistically significant differences.

Results

Patient Baseline Characteristics

Table 1 shows the baseline characteristics of all patients (n = 162), training set patients (n = 113), and testing set patients (n = 49). The mean age of the 162 female breast cancer patients was 50.549 ± 9.563. There were no significant differences in any characteristics between the training and testing sets (all P>0.05).

Table 1 Comparison of Baseline Data Between Training and Testing Sets

Variable	Total (n=162)	Training Set (n=113)	Test Set (n=49)	*P*
Age, years	50.549±9.563	49.779±9.189	52.327±10.155	0.121
Ki-67 index, %	45.000[25.000,67.000]	40.000[25.000,60.000]	50.000[30.000,70.000]	0.270
Histologic grade, n (%)				
I–II	98(60.494)	72(63.717)	26(53.061)	0.203
III	64(39.506)	41(36.283)	23(46.939)	
Shape, n (%)				
Regular	31(19.136)	18(15.929)	13(26.531)	0.115
Irregular	131(80.864)	95(84.071)	36(73.469)	
Fibroglandular type, n (%)				
Scant	21(12.963)	11(9.735)	10(20.408)	0.142
Moderate	23(14.198)	18(15.929)	5(10.204)	
Profuse	118(72.840)	84(74.336)	34(69.388)	
BPE, n (%)				
Mild	121(74.691)	83(73.451)	38(77.551)	0.581
Moderate to severe	41(25.309)	30(26.549)	11(22.449)	
Signal TIC, n (%)				
Inflow type	43(26.543)	29(25.664)	14(28.571)	0.899
Platform type	83(51.235)	58(51.327)	25(51.020)	
Outflow type	36(22.222)	26(23.009)	10(20.408)	
Maximum diameter, mm	25.000[19.000,34.000]	25.000[19.000,32.000]	26.000[20.000,38.000]	0.229
T1 mapping $_{tumor}$	1471.984±169.417	1483.290±173.786	1445.911±155.787	0.199
T2 mapping $_{tumor}$	85.843±11.411	85.107±11.607	87.539±10.757	0.215
ΔT1 mapping $_{tumor}$	431.390[389.250,494.660]	427.080[389.250,483.620]	445.160[390.330,545.730]	0.279

(*Continued*)

https://doi.org/10.2147/BCTT.S594356

Table 1 (Continued).

Variable	Total (n=162)	Training Set (n=113)	Test Set (n=49)	*P*
ADC_{tumor}, 10^{-6}	1.050[0.940,1.180]	1.040[0.910,1.180]	1.080[0.980,1.180]	0.238
ΔT_{tumor}, %	0.699[0.658,0.734]	0.704[0.671,0.735]	0.684[0.625,0.728]	0.034
T1 mapping $_{local}$	1401.090[1310.970,1517.560]	1400.820[1315.220,1517.560]	1418.940[1308.970,1516.380]	0.864
T2 mapping $_{local}$	81.444±13.856	81.123±13.058	82.186±15.516	0.656
ΔT1 mapping $_{local}$	407.600[361.380,482.050]	408.110[372.550,478.940]	394.340[338.040,488.780]	0.431
ADC_{local}, 10^{-6}	0.900[0.790,1.010]	0.900[0.790,1.000]	0.880[0.800,1.010]	0.667
ΔT_{local}, %	0.707[0.659,0.740]	0.707[0.659,0.737]	0.711[0.659,0.754]	0.827

Abbreviations: BPE, Background parenchymal enhancement; TIC, Time-intensity curve; ADC, Apparent diffusion coefficient.

Within the training set, TNBC constituted 15.6% (21/113), with the remaining 84.4% being non-TNBC. Given the limited number of positive samples in the training set, data imbalance could impair the performance of the discriminative model. Therefore, we employed borderline SMOTE to address this imbalance in the training set. After borderline SMOTE processing, the total number of samples was 184. The proportion of the minority class (TNBC) in the training set increased from 15.6% to 50.0%. This resulted in equal representation of breast cancer patients across both groups, with 92 non-TNBC patients and 92 TNBC patients. The data distribution was more balanced, which improved discrimination accuracy (Table 2 and Figure S1A and B). Comparison of clinical data distributions revealed differences between the two groups in clinical characteristics (Ki-67 index and histologic grade), conventional MRI imaging features (BPE), and 10 qMRI imaging variables (all $P<0.05$) (Table 2).

Table 2 Baseline Characteristics Distribution Between the Non-TNBC and TNBC Groups in the Training Set After Borderline SMOTE Processing

Variable	Total (n=184)	Non-TNBC (n=92)	TNBC (n=92)	*P*
Histologic grade, n (%)				
I–II	107(58.152)	67(72.826)	40(43.478)	<0.001
III	77(41.848)	25(27.174)	52(56.522)	
Shape, n (%)				
Regular	40(21.739)	16(17.391)	24(26.087)	0.153
Irregular	144(78.261)	76(82.609)	68(73.913)	
Fibroglandular type, n (%)				
Scant	13(7.065)	9(9.783)	4(4.348)	0.057
Moderate	42(22.826)	15(16.304)	27(29.348)	
Profuse	129(70.109)	68(73.913)	61(66.304)	
BPE, n (%)				
Mild	150(81.522)	68(73.913)	82(89.130)	0.008
Moderate to severe	34(18.478)	24(26.087)	10(10.870)	
Signal TIC, n (%)				
Inflow type	62(33.696)	25(27.174)	37(40.217)	0.171
Platform type	90(48.913)	49(53.261)	41(44.565)	
Outflow type	32(17.391)	18(19.565)	14(15.217)	
T1 mapping $_{tumor}$	1501.160[1397.659,1618.490]	1477.590[1360.900,1570.310]	1523.948[1445.967,1666.735]	0.013
T2 mapping $_{tumor}$	87.850[80.960,94.821]	84.830[74.810,92.900]	90.800[86.346,97.291]	<0.001
ΔT1 mapping $_{tumor}$	466.990[406.070,527.700]	421.550[385.370,466.990]	513.829[466.491,557.880]	<0.001
ADC_{tumor} 10^{-6}	1.081[0.980,1.251]	1.020[0.890,1.150]	1.134[1.023,1.326]	<0.001
ΔT_{tumor}, %	0.683[0.657,0.722]	0.717[0.680,0.741]	0.665[0.651,0.686]	<0.001
T1 mapping $_{local}$	1443.239±177.843	1413.079±172.935	1473.398±177.569	0.021

(*Continued*)

https://doi.org/10.2147/BCTT.S594356

Table 2 (Continued).

Variable	Total (n=184)	Non-TNBC (n=92)	TNBC (n=92)	*P*
T2 mapping $_{local}$	82.661±11.663	80.418±13.494	84.905±8.939	0.009
ΔT1 mapping $_{local}$	432.685[383.300,518.906]	405.250[364.300,473.330]	491.852[403.318,550.186]	<0.001
ADC_{local},10^{-6}	0.940[0.840,1.060]	0.880[0.770,0.990]	0.993[0.910,1.114]	<0.001
ΔT_{local}, %	0.689[0.657,0.720]	0.710[0.670,0.743]	0.682[0.651,0.705]	<0.001
Age, years	50.000[45.000,55.000]	50.000[45.000,55.000]	51.000[45.000,54.000]	0.742
Ki-67 index, %	60.000[35.000,75.979]	35.000[20.000,55.000]	75.000[62.768,79.848]	<0.001
Maximum diameter, mm	25.000[19.000,31.000]	25.000[19.000,32.000]	25.000[20.000,31.000]	0.733

Abbreviations: SMOTE, Synthetic minority over-sampling technique; TNBC, Triple-negative breast cancer; BPE, Background parenchymal enhancement; TIC, Time-intensity curve; ADC, Apparent diffusion coefficient.

Model Construction

Development of the Clinical-Conventional MRI Model

Two statistically significant clinical variables (Ki-67 index and histologic grade) and one conventional MRI imaging variable (BPE) identified in the baseline analysis were incorporated into a multivariable logistic regression analysis to further investigate independent influencing factors on TNBC. Results indicated that Ki-67 index and BPE were factors influencing TNBC (Table 3). A clinical-conventional MRI model was constructed based on these two indicators, and its performance was evaluated. ROC analysis revealed an area under the curve (AUC) value of 0.896 (0.848–0.931) for the clinical-conventional MRI model (Figure 2A). DCA further confirmed that this model demonstrated a favorable net benefit in clinical applications (Figure 2B).

Construction of qMRI Model

Baseline comparisons revealed differences in 10 qMRI imaging variables between non-TNBC and TNBC. We first performed multicollinearity analysis on these 10 significant qMRI variables and excluded variables with VIF > 10. The remaining four variables (ADC_{tumor}, ADC_{local}, T2 $mapping_{local}$, and T2 $mapping_{tumor}$) were included in subsequent multivariable analysis (Table S2). Multivariable logistic regression results indicated that ADC_{tumor} and T2 mapping $_{tumor}$ were associated with TNBC (Table 4). Based on these two variables, a qMRI model was constructed. ROC analysis showed an AUC value of 0.781 (0.718–0.853) for the qMRI model (Figure 3A). DCA indicated a favorable clinical net benefit (Figure 3B).

Construction of the Radiomics Model

All lesions were manually segmented using the 3D Slicer open-source platform, and 837 radiomics features were extracted. The 837 features were subjected to LASSO regression analysis. Using λ = 0.061 (standard error of the left minimum

Table 3 Influence of Clinical-Conventional MRI Variables on TNBC Based on Multivariable Logistic Regression

Variable	OR (95% CI)	*P*
(Intercept)	0.014(0.003–0.047)	<0.001
Ki-67 index	1.085(1.061–1.114)	<0.001
Histologic grade, n (%)		
I–II	Reference	
III	1.012(0.414–2.395)	0.979
BPE, n (%)		
Mild	Reference	
Moderate to severe	0.216(0.073–0.601)	0.004

Abbreviations: MRI, Magnetic resonance imaging; TNBC, Triple-negative breast cancer; BPE, Background parenchymal enhancement; OR, Odds ratio; CI, Confidence interval.

https://doi.org/10.2147/BCTT.S594356

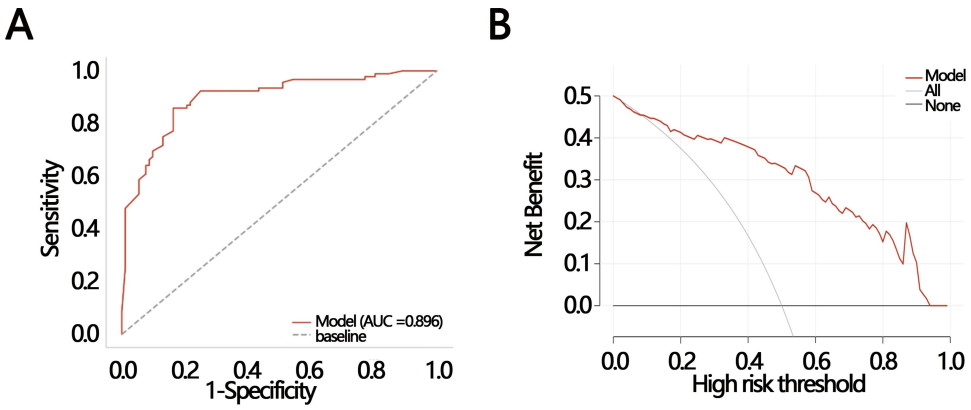

Figure 2 Performance evaluation of the clinical-conventional MRI model based on ROC (**A**) and DCA (**B**) analyses.
Abbreviations: MRI, Magnetic resonance imaging; ROC, Receiver operating characteristic curve analysis; DCA, Decision curve analysis; AUC, Area under the curve.

distance), 17 radiomics features were selected (Figure 4A and B). The importance of these 17 features was further ranked using XG Boost and Random Forest algorithms. The overlapping features within the top ten of both algorithms were considered key radiomics features (cluster shade, dependence entropy, kurtosis, 90th percentile, small area low gray level emphasis, low gray level run emphasis, small area emphasis, strength, and gray level variance) (Table S3 and Figure 4C). The Rad score was calculated based on the LASSO regression coefficients of these nine key indicators: Rad score = 0.048*Cluster shade - 0.239*Dependence entropy - 0.146*Kurtosis + 0.439*90 Percentile + 0.226*Small area low gray level emphasis +. - 0.146*Gray level variance. The TNBC group exhibited a significantly higher Rad score than the non-TNBC group (P<0.001) (Figure 4D). Ultimately, a radiomics model was constructed based on these nine features. ROC analysis revealed an AUC value of 0.905 (0.841–0.951) for the radiomics model, demonstrating excellent discriminatory capability (Figure 5A). DCA further confirmed the model's favorable net benefit in clinical application (Figure 5B).

Construction of Integrated Models and Performance Validation

After evaluating the performance of three independent models, including clinical-conventional MRI, qMRI model, and radiomics model, we further constructed multiple integrated models based on the baseline model (clinical-conventional MRI model) and compared the clinical efficacy of different models across the training processed by borderline SMOTE and original testing sets (Table 5). ROC results showed that in the training set processed by borderline SMOTE, the AUC values for integrated model 1, integrated model 2, and the full integrated model were 0.936 (0.898–0.964), 0.972 (0.949–0.988), and 0.986 (0.973–0.998). The full integrated model exhibited the highest AUC (all DeLong tests P<0.05) (Table 5 and Figure 6A). The model performance comparison results based on data delineated by independent readers were similar to those from the training set processed by borderline SMOTE (Figure 6B).

We conducted internal validation on the original training set using 10-fold nested cross-validation (Table 6). Based on the nested cross-validation results, integrated model 1 and the baseline model were the two most stable models.

Table 4 Influence of qMRI Variables on TNBC Based on Multivariable Logistic Regression

Variable	OR (95% CI)	*P*
(Intercept)	0.000(0.000–0.001)	<0.001
ADC_{tumor}	21.150(1.181–462.890)	0.044
ADC_{local}	5.620(0.220–147.919)	0.296
T2 mapping $_{local}$	0.970(0.922–1.018)	0.223
T2 mapping $_{tumor}$	1.106(1.048–1.173)	<0.001

Abbreviations: qMRI, Quantitative magnetic resonance imaging; ADC, Apparent diffusion coefficient; OR, Odds ratio; CI, Confidence interval.

https://doi.org/10.2147/BCTT.S594356

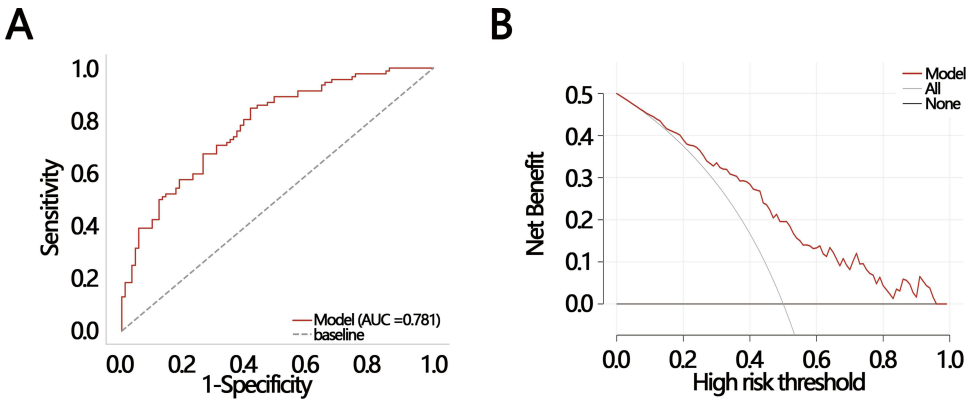

Figure 3 Performance evaluation of the qMRI model based on ROC (**A**) and DCA (**B**) analyses.
Abbreviations: qMRI, Quantitative magnetic resonance imaging; ROC, Receiver operating characteristic curve analysis; DCA, Decision curve analysis; AUC, Area under the curve.

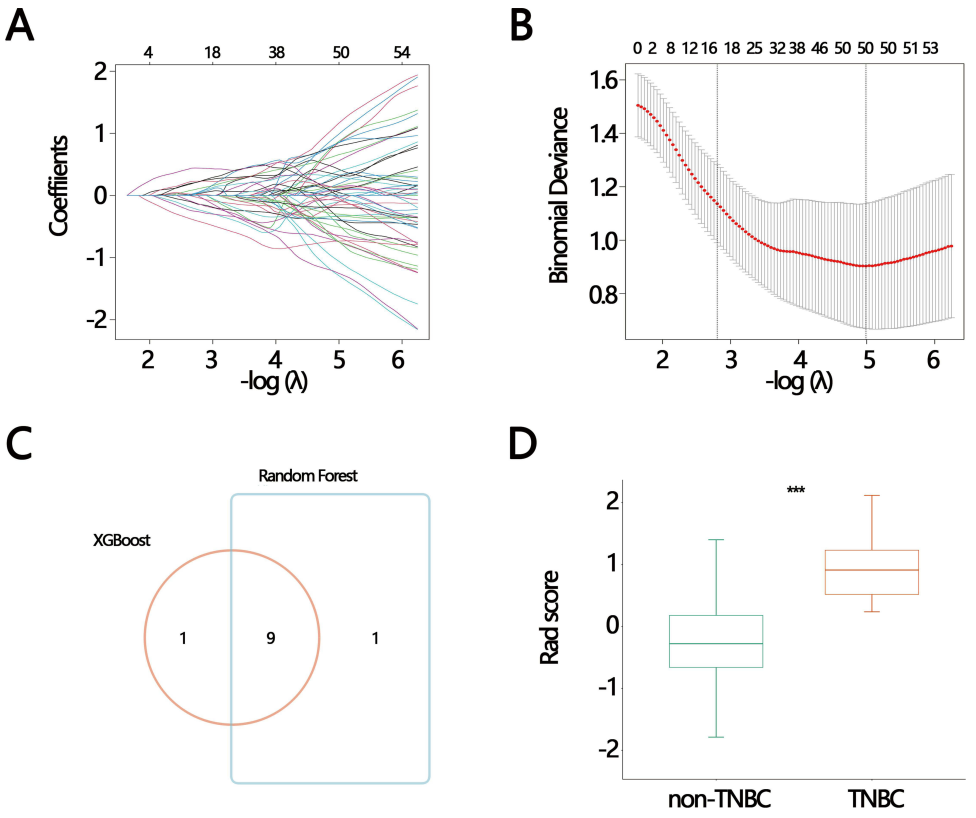

Figure 4 Screening of radiomics features and comparison of Rad scores. (**A**) Coefficient shrinkage patterns across variables. (**B**) A cross-validation curve demonstrating model performance. (**C**) Venn diagram of the top ten important regions for XG Boost and Random Forest algorithms. (**D**) Comparison of the Rad score between the non-TNBC and TNBC groups. ***$P<0.001$.
Abbreviation: TNBC, Triple-negative breast cancer.

A common feature of these models is the minimal difference in AUC between the training and test sets (0.008 for integrated model 1 and 0.010 for the baseline model), with the test set AUC slightly exceeding that of the training set. This indicates strong generalisation ability and the absence of overfitting. However, on the original test set, the AUC values decreased for integrated model 1 (0.827), integrated model 2 (0.680), and the full integrated model (0.718). Only the clinical-conventional MRI model maintained a relatively stable AUC (0.862) (Figure 6C).

https://doi.org/10.2147/BCTT.S594356

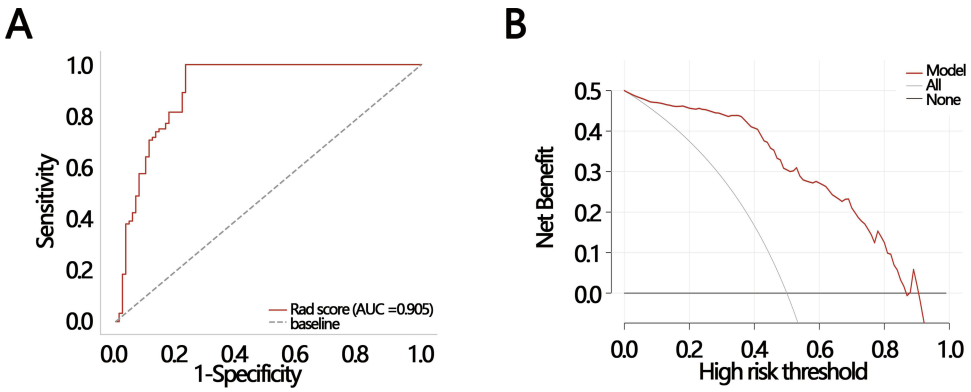

Figure 5 Performance evaluation of radiomics model based on ROC (**A**) and DCA (**B**) analyses.
Abbreviations: ROC, Receiver operating characteristic curve analysis; DCA, Decision curve analysis; AUC, Area under the curve.

Discussion

TNBC is characterized by the absence of ER, PR, and HER2 expression, making endocrine and targeted therapies ineffective and often leading to poor patient outcomes. Chemotherapy, radiotherapy, and surgery are the standard treatments for TNBC. Although TNBC is responsive to chemotherapy, drug resistance and recurrence are common issues leading to treatment failure.[29] Therefore, accurately identifying TNBC before treatment is crucial for developing personalized neoadjuvant chemotherapy regimens and improving patient outcomes. Precise identification of TNBC is essential for achieving "diagnostic-therapeutic integration". This study systematically assessed the value of clinical-conventional MRI variables, qMRI variables, and radiomics features in discriminating TNBC, focusing on the efficacy and stability of multimodal integrated models. The goal is to provide clinicians with a practical decision-making tool.

This study first validated the robust diagnostic capability of the baseline clinical-conventional MRI model. Our results demonstrated that the model integrating Ki-67 index with BPE exhibited excellent and stable discriminatory performance in both training and testing sets (training set AUC: 0.896; testing set AUC: 0.862). Ki-67 index, a key biomarker of cellular proliferation, is highly expressed as a hallmark of TNBC and is closely associated with tumor aggressiveness.[30,31] BPE may be related to TNBC-induced changes in the tumor microenvironment, such as increased angiogenesis and inflammatory responses.[32] Research suggests that a high BPE may serve as an imaging biomarker for a relatively favorable prognosis in TNBC cases undergoing chemotherapy.[33] The robustness of this model indicates that integrating key clinical-pathological indicators with visual assessment features from conventional MRI in clinical practice could provide a reliable and easily scalable diagnostic foundation for TNBC discrimination.

Table 5 ROC Results for the Integrated Model on the Training Set Processed by Borderline SMOTE and Test Set

Feature	AUC	Sensitivity	Specificity	Youdens Index	Accuracy	Delong Test
Training set						
Baseline model	0.896(0.847–0.940)	0.859(0.809–0.964)	0.837(0.711–0.911)	0.696(0.600–0.798)	0.852(0.801–0.900)	/
Integrated model 1	0.936(0.898–0.964)	0.902(0.816–0.962)	0.848(0.773–0.948)	0.750(0.671–0.847)	0.880(0.837–0.924)	0.018
Integrated model 2	0.972(0.949–0.988)	0.870(0.855–0.995)	0.967(0.853–0.979)	0.837(0.791–0.909)	0.929(0.891–0.957)	<0.001
Full integrated model	0.986(0.973–0.998)	0.935(0.883–1.000)	0.946(0.857–0.995)	0.880(0.830–0.957)	0.947(0.913–0.979)	<0.001
Test set						
Baseline model	0.862(0.762–0.953)	1.000(1.000–1.000)	0.762(0.649–0.931)	0.762(0.649–0.867)	0.800(0.694–0.945)	/
Integrated model 1	0.827(0.707–0.990)	1.000(0.697–1.000)	0.643(0.534–1.000)	0.643(0.534–0.973)	0.740(0.601–0.995)	0.495
Integrated model 2	0.680(0.579–0.883)	0.857(0.513–1.000)	0.548(0.318–0.943)	0.405(0.302–0.725)	0.659(0.454–0.878)	0.039
Full integrated model	0.718(0.518–0.934)	0.714(0.500–1.000)	0.786(0.318–0.965)	0.500(0.315–0.897)	0.761(0.388–0.934)	0.182

Notes: Baseline model was clinical-conventional MRI model; integrated model 1 was clinical-conventional MRI model with qMRI parameters; integrated model 2 was clinical-conventional MRI model with radiomics features; and full integrated model was clinical-conventional MRI model integrating all multimodal features.
Abbreviations: SMOTE, Synthetic minority over-sampling technique; ROC, Receiver operating characteristic curve analysis; AUC, Area under the curve; MRI, Magnetic resonance imaging; qMRI, Quantitative MRI.

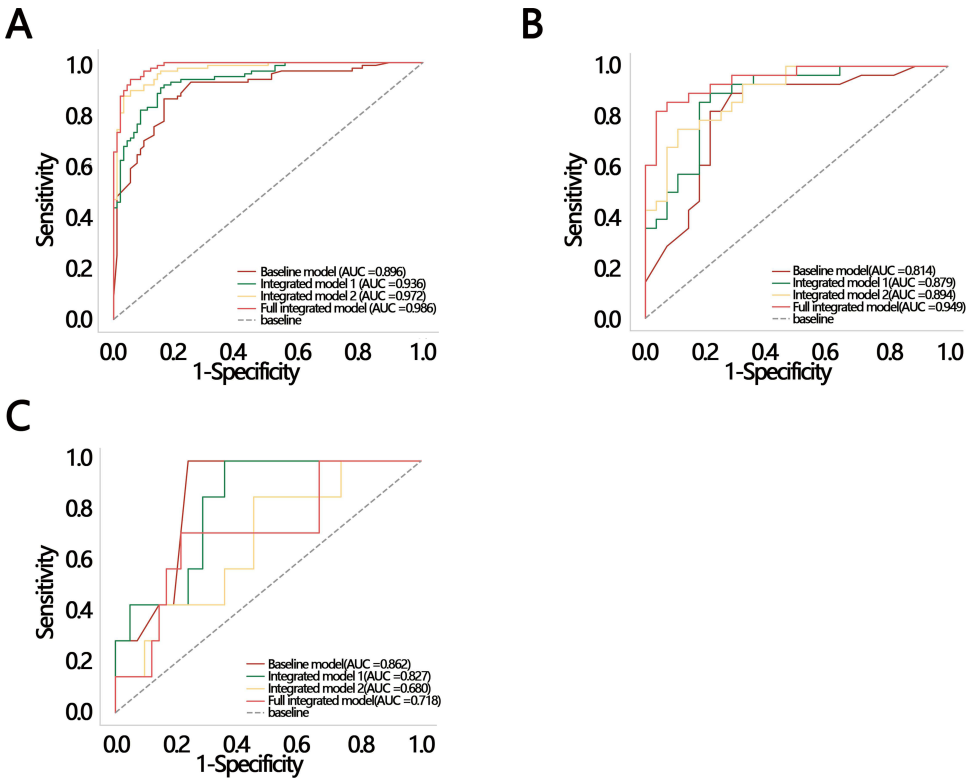

Figure 6 Comparison of integrated model performance in the training set processed by borderline SMOTE (**A**), independent reader annotation data (**B**), and the original test set (**C**).
Notes: Baseline model was a clinical-conventional MRI model; integrated model 1 was a clinical-conventional MRI model with qMRI parameters; integrated model 2 was a clinical-conventional MRI model with radiomics features; and full integrated model was a clinical-conventional MRI model integrating all multimodal features.
Abbreviations: SMOTE, Synthetic minority over-sampling technique; AUC, Area under the curve.

The qMRI model, combining ADC_{tumor} and T2 mapping $_{tumor}$, demonstrated moderate discriminating value in the training set (AUC: 0.781). ADC values reflect water molecule diffusion dynamics, with reduced values typically indicating high tumor cell density and active proliferation characteristics consistent with TNBC biology.[34] However, our research revealed that both ADC_{tumor} and T2 mapping $_{tumor}$ were higher in TNBC patients compared to those with non-TNBC. This could be due to intramural necrosis, which is marked by high signal intensity on T2WI and is closely linked to tumor invasiveness and increased ADC values. Necrotic tumor areas have lower cell density, greater diffusion, signal loss, and higher ADC values on DWI.[35] While qMRI models alone have limited effectiveness, they offer objective, quantitative insights into the tumor's microscopic physical state. Moreover, the changes in the microenvironment that it reveals merit further investigation. Research indicates that an elevated platelet-to-lymphocyte ratio (a marker of systemic inflammation) in breast cancer patients correlates with increased ADC values, suggesting that diffusion-weighted imaging parameters may indirectly reflect changes in the immune microenvironment.[36] Recent imaging studies confirm

Table 6 Internal Validation Performance

Model	Mean AUC for 10 Fold-Nested Cross-Validation Training Set	Mean AUC for 10 Fold-Nested Cross-Validation Test Set
Baseline model	0.876(0.863–0.889)	0.886(0.788–0.985)
Integrated model 1	0.897(0.889–0.905)	0.905(0.823–0.987)
Integrated model 2	0.950(0.941–0.960)	0.899(0.806–0.991)
Full integrated model	0.955(0.946–0.964)	0.876(0.774–0.979)

Notes: Baseline model was clinical-conventional MRI model; integrated model 1 was clinical-conventional MRI model with qMRI parameters; integrated model 2 was clinical-conventional MRI model with radiomics features; and full integrated model was clinical-conventional MRI model integrating all multimodal features.
Abbreviations: AUC, Area under the curve; MRI, Magnetic resonance imaging; qMRI, Quantitative MRI.

https://doi.org/10.2147/BCTT.S594356

that image-based tumour heterogeneity indices effectively identify breast cancer patient subgroups exhibiting a "hot" tumour immune microenvironment (characterised by active immune pathways and extensive immune cell infiltration).[37] The high tumour heterogeneity in TNBC manifests not only at the molecular level but also in the complex composition of its tumour immune microenvironment. Imaging phenotypes are increasingly demonstrating potential to reflect modifiable immune signalling nodes.[38,39]

Studies have shown that radiomics models based on automated image segmentation of DCE-MRI can discriminate TNBC from non-TNBC with an AUC of 0.867.[40] DCE-MRI features deconstruct tumour imaging from multiple dimensions. For instance, cluster shade is frequently employed to evaluate tissue structural heterogeneity and dynamic changes, revealing the distribution of distinct cell types within tissues.[41] Higher cluster shade values indicate more pronounced spatial differences in cell distribution, thereby enhancing tissue heterogeneity.[42] This index exhibits a negative correlation with the density of tumour-infiltrating lymphocytes (eg., CD8+ T cells), potentially reflecting the formation of an immunosuppressive tumour microenvironment to some extent.[43] Small area low gray level emphasis characterises the abundance of small, contiguous regions within tumours composed of low-signal (dark) pixels. Imaging-wise, such small, dark areas often correspond to microscopic necrotic zones, fluid-filled structures, old haemorrhages, or mucin lakes. Elevated values of this metric suggest the presence of numerous scattered micro-low signal structures within the tumour.[44] In our study, the radiomics model exhibited exceptional discriminative ability in the training set with an AUC of 0.905, surpassing clinical models. This fully confirms the significant potential of radiomics in revealing deep image features that are not visible to the human eye and in quantifying tumor internal heterogeneity.[45]

In the training set processed by borderline SMOTE, the integrated models, particularly the integrated model 2 combining the clinical-conventional MRI model with the radiomics model and the fully integrated model, achieved AUC values of 0.972 and 0.986, significantly outperforming any single model. This result strongly demonstrated that clinical, quantitative, and radiomics features indeed depict the characteristics of TNBC from different perspectives, with their information being highly complementary and non-redundant. This aligns with the current trend in precision oncology towards moving from single biomarkers to multi-omics integration.[46] Ideally, integrating this multidimensional information can construct a more robust diagnostic model that better approximates reality. However, the rigor of scientific research requires validating models on unseen data. Performance evaluation on the test set revealed a significant decline in accuracy for all complex integrated models, with only the baseline clinical-conventional MRI model maintaining optimal stability (AUC: 0.862). This phenomenon represents one of the core findings of this study, profoundly illustrating a critical trade-off between model robustness (or generalization ability) and complexity in medical model development. The cause may be attributed to sample size limitations. The relatively small number of TNBC cases (n=28) in this study, combined with the large parameter space of complex integrated models (especially those incorporating high-dimensional omics features), made them prone to overfitting noise and specific patterns in the training data, resulting in insufficient generalization. From a deeper biological perspective, this risk of overfitting stems not only from excessive statistical parameters but also from the inherent difficulty of small-sample data in reliably supporting cross-scale inference from high-dimensional imaging features to complex molecular networks.[47]

This study successfully validated a clinical-conventional MRI model that demonstrated both high discriminative efficacy and outstanding generalization capability. This model may provide effective and reliable support for clinicians in preoperative TNBC discrimination. Among the included patients with a single mass lesion larger than 1 centimeter (cm), the model achieved high specificity (76.2%) on the original test set based on the optimal diagnostic threshold, with a Youden index of 0.762. This suggests its potential clinical utility within this specific patient population. Although qMRI and radiomics models show immense potential, and multi-model integration is theoretically a future direction, their clinical application still faces severe challenges in generalization capability. Our findings caution against blindly pursuing model complexity, emphasizing the importance of simplicity, interpretability, and reproducibility on independent datasets. This focus on model robustness and generalisability represents a common challenge across the entire field of AI in medical imaging. From multimodal image analysis in neurodegenerative diseases to AI-assisted diagnosis in oncology, model validation, reproducibility, and stability across diverse populations and acquisition protocols remain primary barriers to clinical translation.[48] Placing our research findings within this interdisciplinary context further underscores the universal value of conducting prospective, multicentre studies and developing standardised, shareable

data platforms for advancing AI models from research into clinical practice. There were several limitations: First, this single-center retrospective study inherently carries selection bias. Second, the limited TNBC sample size may be insufficient for adequately training and validating high-dimensional integrated models. Finally, model performance declined in the test set, indicating that its generalization capability requires further improvement. Future research should focus on conducting prospective, multicenter, large-sample cohort studies to provide a robust data foundation for complex models; developing more advanced feature selection and regularization algorithms to construct leaner, more robust integrated models; and ultimately conducting external independent validation to objectively assess their practical value in real-world clinical settings.

Conclusion

This study confirmed that the clinical-conventional MRI model integrating Ki-67 index and BPE exhibited optimal robustness and generalization capability in distinguishing TNBC. Moreover, the radiomic features extracted in this study-such as cluster shadows-quantify tumour microheterogeneity, offering insights into the imaging-pathology correlation in TNBC. However, despite demonstrating superior efficacy in the training set, the fusion model exhibited a significant decline in performance on the independent test set. This suggests a critical trade-off between model complexity and generalisation capability when working with limited samples. Future research must validate the model's generalisability through rigorous statistical testing in larger, multicentre datasets. Subgroup analyses should identify optimal patient populations for the model, thereby advancing the robust translation of multiparametric MRI fusion models from research to clinical practice.

Data Sharing Statement

The datasets generated during and/or analyzed during the current study are available from the corresponding author [Dandan Lin] on reasonable request.

Ethics Approval

The Ethics Committee of Longyan First Affiliated Hospital of Fujian Medical University deemed that this research is based on open-source data, so the need for ethics approval was waived.

Funding

This study was sponsored by Fujian Province Natural Science Foundation (Grant number: 2022J011501).

Disclosure

The authors report no conflict of interest.

References

1. Wilkinson L, Gathani T. Understanding breast cancer as a global health concern. *Br J Radiol*. 2022;95(1130):20211033. doi:10.1259/bjr.20211033
2. Yin L, Duan JJ, Bian XW, Yu SC. Triple-negative breast cancer molecular subtyping and treatment progress. *Breast Cancer Res*. 2020;22(1):61. doi:10.1186/s13058-020-01296-5
3. Pont M, Marques M, Sorolla A. Latest Therapeutical Approaches for Triple-Negative Breast Cancer: from Preclinical to Clinical Research. *Int J Mol Sci*. 2024;25(24):13518. doi:10.3390/ijms252413518
4. Kumar H, Gupta NV, Jain R, et al. A review of biological targets and therapeutic approaches in the management of triple-negative breast cancer. *J Adv Res*. 2023;54:271–292. doi:10.1016/j.jare.2023.02.005
5. Popa MT, Noditi A, Peleasa TM, Stoleru S, Blidaru A. Breast Cancer: a Heterogeneous Pathology. Prognostic and Predictive Factors - A Narrative Review. *Chirurgia*. 2025;120(1):32–47. doi:10.21614/chirurgia.3100
6. Raman R, Debata S, Govindarajan T, Kumar P. Targeting Triple-Negative Breast Cancer: resistance Mechanisms and Therapeutic Advancements. *Cancer Med*. 2025;14(9):e70803. doi:10.1002/cam4.70803
7. Bhalla K, Xiao Q, Luna JM, et al. Radiologic imaging biomarkers in triple-negative breast cancer: a literature review about the role of artificial intelligence and the way forward. *BJR Artif Intell*. 2024;1(1):ubae016. doi:10.1093/bjrai/ubae016
8. Huang Y, Wang X, Cao Y, et al. Multiparametric MRI model to predict molecular subtypes of breast cancer using Shapley additive explanations interpretability analysis. *Diagn Interv Imaging*. 2024;105(5):191–205. doi:10.1016/j.diii.2024.01.004
9. Son J, Lee SE, Kim EK, Kim S. Prediction of breast cancer molecular subtypes using radiomics signatures of synthetic mammography from digital breast tomosynthesis. *Sci Rep*. 2020;10(1):21566. doi:10.1038/s41598-020-78681-9

10. Valdora F, Houssami N, Rossi F, Calabrese M, Tagliafico AS. Rapid review: radiomics and breast cancer. *Breast Cancer Res Treat*. 2018;169(2):217–229. doi:10.1007/s10549-018-4675-4
11. Bickelhaupt S, Paech D, Kickingereder P, et al. Prediction of malignancy by a radiomic signature from contrast agent-free diffusion MRI in suspicious breast lesions found on screening mammography. *J Magn Reson Imaging*. 2017;46(2):604–616. doi:10.1002/jmri.25606
12. Leithner D, Horvat JV, Marino MA, et al. Radiomic signatures with contrast-enhanced magnetic resonance imaging for the assessment of breast cancer receptor status and molecular subtypes: initial results. *Breast Cancer Res*. 2019;21(1):106. doi:10.1186/s13058-019-1187-z
13. Zhou J, Tan H, Li W, et al. Radiomics Signatures Based on Multiparametric MRI for the Preoperative Prediction of the HER2 Status of Patients with Breast Cancer. *Acad Radiol*. 2021;28(10):1352–1360. doi:10.1016/j.acra.2020.05.040
14. Chen H, Min Y, Xiang K, Chen J, Yin G. DCE-MRI Performance in Triple Negative Breast Cancers: comparison with Non-Triple Negative Breast Cancers. *Curr Med Imaging*. 2022;18(9):970–976. doi:10.2174/1573405618666220225090944
15. Bignotti B, Signori A, Valdora F, et al. Evaluation of background parenchymal enhancement on breast MRI: a systematic review. *Br J Radiol*. 2017;90(1070):20160542. doi:10.1259/bjr.20160542
16. Liu L, Yin B, Shek K, et al. Role of quantitative analysis of T2 relaxation time in differentiating benign from malignant breast lesions. *J Int Med Res*. 2018;46(5):1928–1935. doi:10.1177/0300060517721071
17. Sharma U, Agarwal K, Hari S, et al. Role of diffusion weighted imaging and magnetic resonance spectroscopy in breast cancer patients with indeterminate dynamic contrast enhanced magnetic resonance imaging findings. *Magn Reson Imaging*. 2019;61:66–72. doi:10.1016/j.mri.2019.05.032
18. Mao X, Zou X, Yu N, Jiang X, Du J. Quantitative evaluation of intravoxel incoherent motion diffusion-weighted imaging (IVIM) for differential diagnosis and grading prediction of benign and malignant breast lesions. *Medicine*. 2018;97(26):e11109. doi:10.1097/MD.0000000000011109
19. Hagiwara A, Warntjes M, Hori M, et al. SyMRI of the Brain: rapid Quantification of Relaxation Rates and Proton Density, With Synthetic MRI, Automatic Brain Segmentation, and Myelin Measurement. *Invest Radiol*. 2017;52(10):647–657. doi:10.1097/RLI.0000000000000365
20. Truhn D, Schrading S, Haarburger C, Schneider H, Merhof D, Kuhl C. Radiomic versus Convolutional Neural Networks Analysis for Classification of Contrast-enhancing Lesions at Multiparametric Breast MRI. *Radiology*. 2019;290(2):290–297. doi:10.1148/radiol.2018181352
21. Nicosia L, Bozzini AC, Ballerini D, et al. Radiomic Features Applied to Contrast Enhancement Spectral Mammography: possibility to Predict Breast Cancer Molecular Subtypes in a Non-Invasive Manner. *Int J Mol Sci*. 2022;23(23):15322. doi:10.3390/ijms232315322
22. Song SE, Woo OH, Cho Y, Cho KR, Park KH, Kim JW. Prediction of Axillary Lymph Node Metastasis in Early-stage Triple-Negative Breast Cancer Using Multiparametric and Radiomic Features of Breast MRI. *Acad Radiol*. 2023;30(Suppl 2):S25–S37. doi:10.1016/j.acra.2023.05.025.
23. The Society of Breast Cancer China Anti-Cancer Association BOGotOBotCMA. Guidelines for breast cancer diagnosis and treatment by China Anti-cancer Association (2024 edition). *China Oncology*. 2023;33(12):1092–1186. doi:10.19401/j.cnki.1007-3639.2023.12.004
24. Zhu X, Chen L, Huang B, et al. The prognostic and predictive potential of Ki-67 in triple-negative breast cancer. *Sci Rep*. 2020;10(1):225. doi:10.1038/s41598-019-57094-3
25. Yuen S, Monzawa S, Yanai S, et al. The association between MRI findings and breast cancer subtypes: focused on the combination patterns on diffusion-weighted and T2-weighted images. *Breast Cancer*. 2020;27(5):1029–1037. doi:10.1007/s12282-020-01105-z
26. Nielsen TO, Leung SCY, Rimm DL, et al. Assessment of Ki67 in Breast Cancer: updated Recommendations From the International Ki67 in Breast Cancer Working Group. *J Natl Cancer Inst*. 2021;113(7):808–819. doi:10.1093/jnci/djaa201
27. van Griethuysen JJM, Fedorov A, Parmar C, et al. Computational Radiomics System to Decode the Radiographic Phenotype. *Cancer Res*. 2017;77(21):e104–e107. doi:10.1158/0008-5472.CAN-17-0339
28. Kim JH, Choi JW, Kwon YS, Kang SS. Predictive model for difficult laryngoscopy using machine learning: retrospective cohort study. *Braz J Anesthesiol*. 2022;72(5):622–628. doi:10.1016/j.bjane.2021.06.016
29. Subhan MA, Torchilin VP. Advances in siRNA Drug Delivery Strategies for Targeted TNBC Therapy. *Bioengineering*. 2024;11(8):830. doi:10.3390/bioengineering11080830
30. Srivastava P, Wang T, Clark BZ, et al. Clinical-pathologic characteristics and response to neoadjuvant chemotherapy in triple-negative low Ki-67 proliferation (TNLP) breast cancers. *NPJ Breast Cancer*. 2022;8(1):51. doi:10.1038/s41523-022-00415-z
31. Wu Q, Ma G, Deng Y, et al. Prognostic Value of Ki-67 in Patients With Resected Triple-Negative Breast Cancer: a Meta-Analysis. *Front Oncol*. 2019;9:1068. doi:10.3389/fonc.2019.01068
32. Duong KS, Rubner R, Siegel A, Adam R, Ha R, Maldjian T. Machine Learning Assessment of Background Parenchymal Enhancement in Breast Cancer and Clinical Applications: a Literature Review. *Cancers*. 2024;16(21):3681. doi:10.3390/cancers16213681
33. Xu C, Yu J, Wu F, et al. Erratum: high-background parenchymal enhancement in the contralateral breast is an imaging biomarker for favorable prognosis in patients with triple-negative breast cancer treated with chemotherapy. *Am J Transl Res*. 2023;15(7):4970.
34. Molinari C, Clauser P, Girometti R, et al. MR mammography using diffusion-weighted imaging in evaluating breast cancer: a correlation with proliferation index. *Radiol Med*. 2015;120(10):911–918. doi:10.1007/s11547-015-0527-z
35. Razek AA, Gaballa G, Denewer A, Nada N. Invasive ductal carcinoma: correlation of apparent diffusion coefficient value with pathological prognostic factors. *NMR Biomed*. 2010;23(6):619–623. doi:10.1002/nbm.1503
36. Dai X, Shen Y, Gao Y, Huang G, Lin B, Liu Y. Correlation study between apparent diffusion coefficients and the prognostic factors in breast cancer. *Clin Radiol*. 2023;78(5):347–355. doi:10.1016/j.crad.2022.11.013
37. Teng X, Zhang J, Lai Q, et al. Tumor heterogeneity index from DCE-MRI for AKT-inhibition responder identification and reveals hot immune microenvironment for patients with breast cancer: a multi-omics analysis of I-SPY2 trial. *Breast Cancer Res*. 2026;28(1):39. doi:10.1186/s13058-026-02219-6
38. Kudelova E, Smolar M, Holubekova V, et al. Genetic Heterogeneity, Tumor Microenvironment and Immunotherapy in Triple-Negative Breast Cancer. *Int J Mol Sci*. 2022;23(23):14937. doi:10.3390/ijms232314937
39. Narote S, Desai SA, Patel VP, Deshmukh R, Raut N, Dapse S. Identification of new immune target and signaling for cancer immunotherapy. *Cancer Genet*. 2025;294–295:57–75. doi:10.1016/j.cancergen.2025.03.004
40. Ma M, Gan L, Jiang Y, et al. Radiomics Analysis Based on Automatic Image Segmentation of DCE-MRI for Predicting Triple-Negative and Nontriple-Negative Breast Cancer. *Comput Math Methods Med*. 2021;2021:2140465. doi:10.1155/2021/2140465
41. Li Z, Huang H, Wang C, et al. DCE-MRI radiomics models predicting the expression of radioresistant-related factors of LRP-1 and survivin in locally advanced rectal cancer. *Front Oncol*. 2022;12:881341. doi:10.3389/fonc.2022.881341

42. Li Z, Zhao Z, Wang C, et al. Association Between DCE-MRI Perfusion Histogram Parameters and EGFR and VEGF Expressions in Different Lauren Classifications of Advanced Gastric Cancer. *Pathol Oncol Res*. 2021;27:1610001. doi:10.3389/pore.2021.1610001
43. Huang H, Li Z, Xia Y, et al. Association between radiomics features of DCE-MRI and CD8(+) and CD4(+) TILs in advanced gastric cancer. *Pathol Oncol Res*. 2023;29:1611001. doi:10.3389/pore.2023.1611001
44. Abtan RA, Al-Saleh AH, Mohamed HJ, Abbas HK, Alzuky A. Texture Features of Grey Level Size Zone Matrix for Breast Cancer Detection. *Iraqi J Sci*. 2023;64(1):492–502. doi:10.24996/ijs.2023.64.1.43
45. Gillies RJ, Kinahan PE, Hricak H. Radiomics: images Are More than Pictures, They Are Data. *Radiology*. 2016;278(2):563–577. doi:10.1148/radiol.2015151169
46. Yasmin A, Jha R, Passi A, et al. Emerging biomarkers in breast cancer: translational and multi-omics perspectives in precision oncology. *Biomarkers*. 2025;30(7):516–540. doi:10.1080/1354750X.2025.2591717
47. Ubaid S, Kushwaha R, Kashif M, Singh V. Comprehensive analysis of oncogenic determinants across tumor types via multi-omics integration. *Cancer Genet*. 2025;298–299:44–62. doi:10.1016/j.cancergen.2025.08.010
48. Xu J, Gao C, Zhang J, et al. Advancements in Imaging Technologies and AI Integration for Neurodegenerative Disease Management: a Narrative Review. *Mol Imaging*. 2025;24:15353508251393056. doi:10.1177/15353508251393056